CB-Note 312

Technical report: $\eta\pi$ P-Wave in the $\pi^-\pi^0\eta$ Channel of $\bar{p}n$ Annihilation at Rest

K. Hüttmann and W. Dünnweber
Sektion Physik, Universität München, D-85748 Garching

April 10, 1997

Contents

1 Introduction

The $\pi^-\ \pi^0\eta$ final state of $\bar{\mathrm{p}}\mathrm{n}$ annihilation was studied with 200 MeV/c antiproton stopped in a liquid deuterium target. Evidence for the $\eta\pi$ P-wave, which has the exotic quantum numbers $\mathrm{I^G(J^{PC})} = 1^-(1^{-(+)})$, is the most interesting aspect of this work. The present annihilation channel is very sensitive to $\eta\pi$ P-wave contributions because only very few other resonances are present. Selection rules exclude isospin I = 0 for any two-meson combination and, in addition, for S-wave annihilation, any $\mathrm{J^P} = 0^+$ intermediate resonance in this channel. As a result, the Dalitz plot has a rather simple structure where only bands from $\rho^-(770) \to \pi^0\pi^-$ and $\mathrm{a_0^{-/0}}(1320) \to \eta\pi^{-/0}$ are prominent, such that the $\eta\pi$ P-wave becomes visible by interferences with these bands.

This note summarizes the analysis of the reaction $\bar{\mathrm{p}}\mathrm{d} \to \pi^-\pi^0\eta + \mathrm{p_{spectator}}$. It uses $8.2 \cdot 10^6$ 1-prong events recorded in the CB beam times of may and October 1991 and June 1994. In a previous exploratory study of only the 1991 data, similar results were obtained for the main points of the present work. The final sample after data selection, including a 100 MeV/c cut on spectator momentum, consists of 52 576 events of which less than 1% are attributed to background.

The partial wave analysis shows that the annihilation channel is dominated by $\rho^-(770)$ and $\mathrm{a_2^{-/0}}(1320)$ production from the $\bar{\mathrm{p}}\mathrm{n}$ S-wave and, by about 30%, P-wave. (Only $^3\mathrm{S}_1$ and $^1\mathrm{P}_1$ are allowed by G-parity). In addition, the analysis definitely requires a $\mathrm{J^P} = 1^-$ $\eta\pi$ intermediate state, which contributes about 10% of the total intensity in the present Dalitz plot. A Breit-Wigner parametrization yields $\mathrm{m} = (1400 \pm 20 \pm 10)$ MeV/c and $\Gamma = (310 \pm 50^{+40}_{-20})$ MeV/c^2.

2 Data Selection

2.1 Preselection

In the experiment, the 1-prong trigger demanded at most one hit in the outer PWC and one or two hits in the JDC layers 21 or 22. The enrichment of 1-prong events with respect to all annihilations in deuterium is estimated (by comparison of the relevant branching ratios) to amount to a factor of 14.

All 1-prong events recorded in three beam times with a liquid deuterium target, as listed in Table 1, were reconstructed at CERN in April 1996 with use of the CB program LOCATER 2.00/01, which involves the Fast-Fuzzy algorithm for charged-particle tracking. Both, photon and charged-particle calibrations are identical to those used for the paper on $\bar{\mathrm{p}}\mathrm{d} \to \pi^-\pi^0\pi^0 + \mathrm{p_{spectator}}$ [4].

In the first selection step we require 1 (and only 1) golden track, defined by demanding at least 15 hits in the JDC with at least 1 hit in the first three layers as well as in the last three layers, and charge $\mathrm{Q} = -1$. Events with any additional track found by LOCATER (input in the TTKS bank) are removed.

The $\gamma\gamma$ decay mode is used to identify η- and π^0 mesons. Hence 4 unmatched PEDs are required in the barrel. These are selected by the golden-γ criteria. This means that hadronic split-offs are identified by the Taxi algorithm and the corresponding PEDs are dropped. For electromagnetic split-offs, identified with the DOLBY-C program, the corresponding PEDs are dropped as well. The following thresholds were set: E(central crystal) $>$ 13 MeV, E(PED) $>$ 13 MeV, E(cluster) $>$ 14 MeV and $\mathrm{E_1/E_9} < 0.96$. Events for which the central crystal of a PED is of type #13 are not accepted.

Two rough kinematic cuts are applied as shown in Fig.1. A broad window in the $\mathrm{P_{tot}/E_{tot}}$ plane selects events with proper kinematics for an undetected proton with p $<$ 400 MeV/c. (Target radius and wall thicknesses correspond to the range of protons at 90° with p $\approx$ 200 MeV/c). In addition, the missing mass is required to be within a broad window around $\mathrm{m_p} : 400 \cdot 10^3\ \mathrm{MeV^2/c^4} \leq 1400 \cdot 10^3\ \mathrm{MeV^2/c^4}$.

2.2 Kinematic Fit

Kinematic fitting with the 4-momenta extracted from the TTKS bank led to pulls which showed systematic deviations from the $\sigma = 1$ normal distribution. Application of the corrections listed in Table 2 resulted in the pulls for the hypothesis $\pi^-\pi^0\eta\mathrm{p_{spect}}$ shown in Fig.2. It is noted that a smaller offset of (1/transverse momentum) is needed for the new JDC than for the old one(Table 2), in accordance with other studies.

In a step, all events that passed the preselection were subjected to a 1C-fit according to the hypothesis $\pi^-4\gamma\mathrm{p_{spect}}$. The confidence level (Fig.3, lhs.) was required to be above 3%. Thereafter a 3C-fit was applied to select the channel $\pi^-\,\pi^0(\to\,\gamma\gamma)\,\eta(\to\,\gamma\gamma)\mathrm{p_{spect}}$. The $\gamma\gamma$ combinations were chosen to obtain the best confidence levels (Fig.3, rhs.) better than 5%. For background discrimination, CL($\pi^-\pi^0\pi^0\mathrm{p_{spect}}$) <5% and CL($\pi^-\eta\eta\mathrm{p_{spect}}$) $<$ CL($\pi^-\pi^0\eta\mathrm{p_{spect}}$) was required. The momentum distribution of the spectator proton

after kinematic fitting is shown in Fig.4. To enable treatment of the proton as a spectator in the analysis below, its momentum was required to be less than 100 MeV/c. After this final cut a total of 52 576 events is left as the final sample. Its confidence level distribution is rather flat (dark histogram in Fig.3). Table 3 shows the effects of the selection steps on statistics.

The purity of the data becomes apparent when the hypothesis $\pi^-\pi^0\eta p_{spect}$ is replaced by $\pi^-\eta\gamma\gamma p_{spect}$ in the above selection procedure. The $\gamma\gamma$ invariant mass spectrum (Fig.5) shows a rather small background below the π^0 peak. A linear fit yields a contribution to the π^0 intensity of $(\ 0.4 \pm 0.1)\%$, which may be taken as upper limit for background contained in the final sample (cf. Monte Carlo studies below).

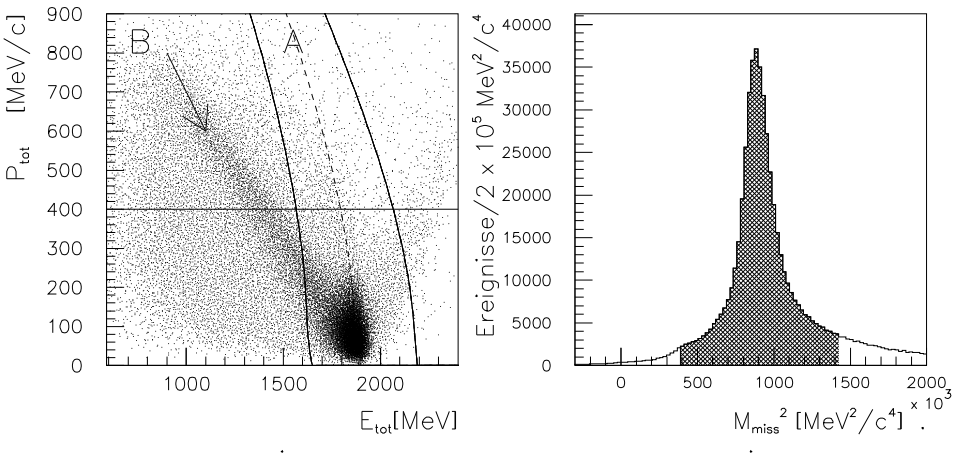

Figure 1: Total momentum versus total energy for $\bar{p}d$ events with one golden track and 4 golden gammas. The correct kinematics for events with a missing (spectator) proton is represented by parabola A. The kinematic window for preselection is defined by the two parabolas (full lines) that correspond to the missing mass window marked in the r.h.s. spectrum and by $P_{tot} < 400\,\mathrm{MeV/c}$.

criterium	May 91	October 91	June 94
1-prong triggered events	535.091	2.476.325	5.197.960
1 golden track, Q= -1	242.264	1.058.565	2.860.221
4 golden gammas	45.837	208.410	540.377
no PED in crystal #13	43.090	195.860	507.977
missing mass window	33.745	150.209	404.058
$P_{tot} < 400$ MeV/c	32.824	146.257	394.907

Table 1: preselection steps

quantity	May 91	October 91	June 94
$\Delta\Psi$	1.3	1.3	1.2
$\Delta 1/P_{xy}$	2.0	2.2	1.8
$(1/P_{xy})_{offset}$	-1/18 GeV	-1/18 GeV	-1/60 GeV
$\Delta tan(\lambda)$	1.3	1.3	1.2

Table 2: correction factors used for the kinematic fit

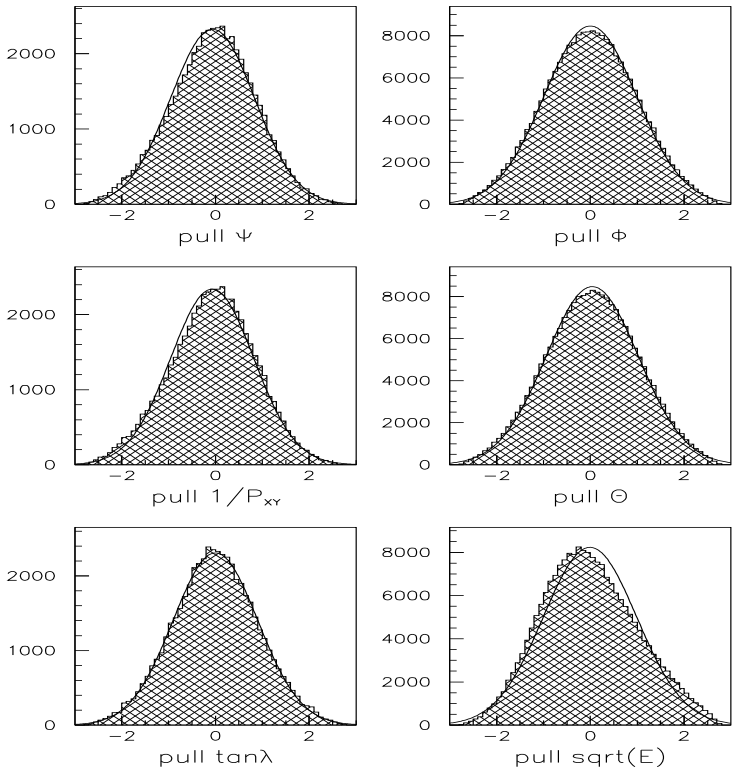

Figure 2: Pulls of the kinematic 3C fit for $\pi^-\pi^0(\rightarrow\gamma\gamma)\eta(\rightarrow\gamma\gamma)p_{spec}$, after corrections according to Table 2, for charged particle data (left) and for photons (right). Shown for comparison are normal distributions with $\sigma = 1$

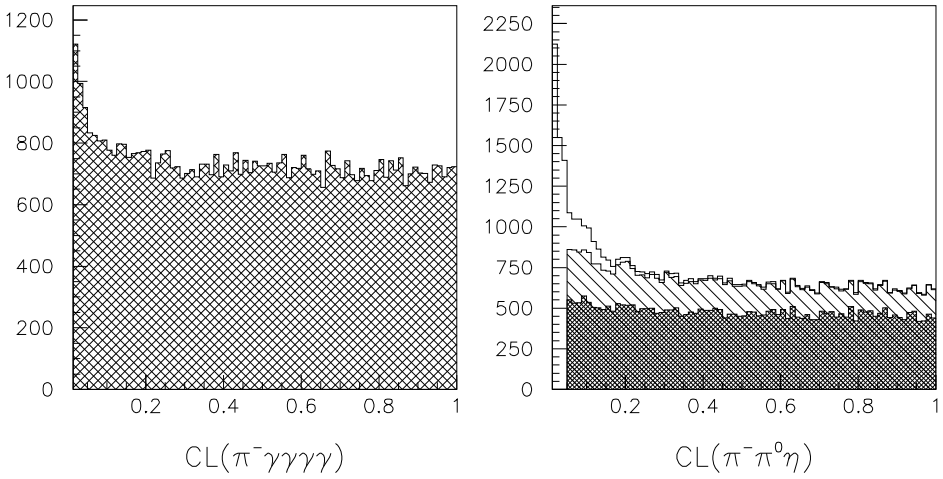

Figure 3: Distribution of confidence levels for the hypothesis $\pi^- 4\gamma p_{spec}$ (left hand side) and $\pi^-\pi^0\eta p_{spec}$ (right hand side). The hatched histogram shows the CL distribution after application of the anticuts on background (see Tab. 3). The dark histogram shows the CL distribution for the final sample, for which $P_{spec} < 100\,\mathrm{MeV/c}$.

criterium	May 91	October 91	June 94
$\mathrm{CL}(\pi^- 4\gamma) > 3\%$			
$\mathrm{CL}(\pi^-\pi^0\eta) > 5\%$	4.407	18.997	52.123
$\mathrm{CL}(\pi^-\pi^0\pi^0) < 5\%$	4.327	18.620	51.230
$\mathrm{CL}(\pi^-\eta\eta) < \mathrm{CL}(\pi^-\pi^0\eta)$	4.308	18.533	50.996
$p_{spec} < 100$ MeV/c	**3.033**	**13.286**	**36.257**

Table 3: Selection steps of the kinematic fit

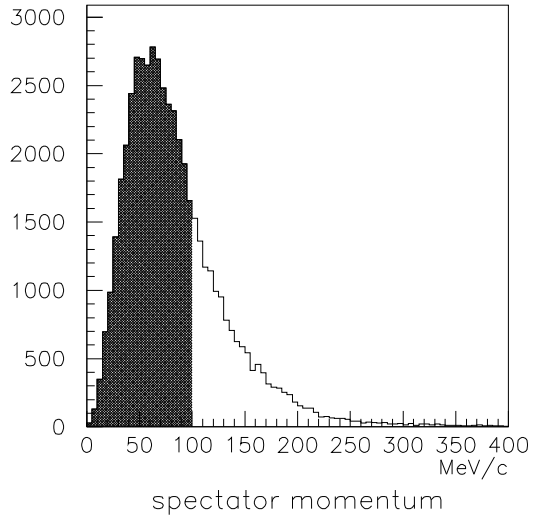

Figure 4: Spectrum of the spectator momentum after the 3C-fit. The hatched area corresponds to the final sample.

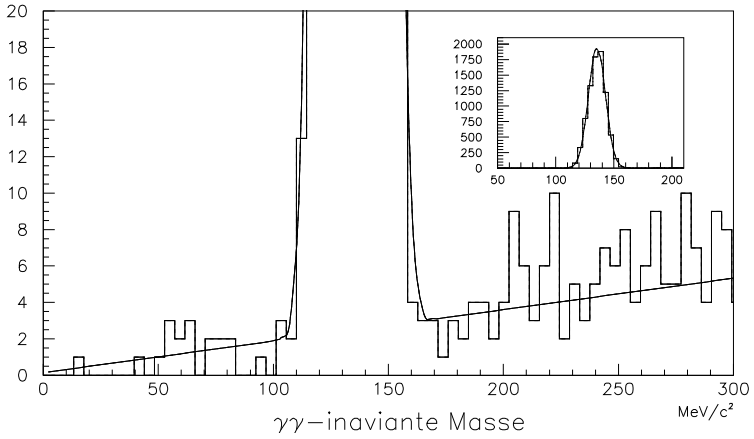

Figure 5: $\gamma\gamma$ invariant mass for the hypothesis $\pi^-\eta\gamma\gamma p_{spec}$ (see text)

2.3 Dalitz Plot

Because of the spectator momentum distribution, the Dalitz plot of the present annihilation channel is in principle a superposition of DPs with slightly different phase space boundaries. Washed-out angular distributions can result from this superposition. However, as shown in Fig.6, the effect is very small for $P_{spect} < 100$ MeV/c. It is smaller or comparable to the experimental resolution (see Monte Carlo studies below) and negligibly small compared to the width of any structure and to the bin size used below. This justifies the representation of all events with $P_{spect} < 100$ MeV/c in a single DP.

All 52 576 events that passed the data selection enter in the DP (Fig. 7) and its projections (Fig. 8). This DP is characterized by a simple structure with a dominant diagonal $\rho^-(770)$ band and two weak orthogonal bands in the region of the $a_2(1320)$. The latter show modulations typical of interference effects.

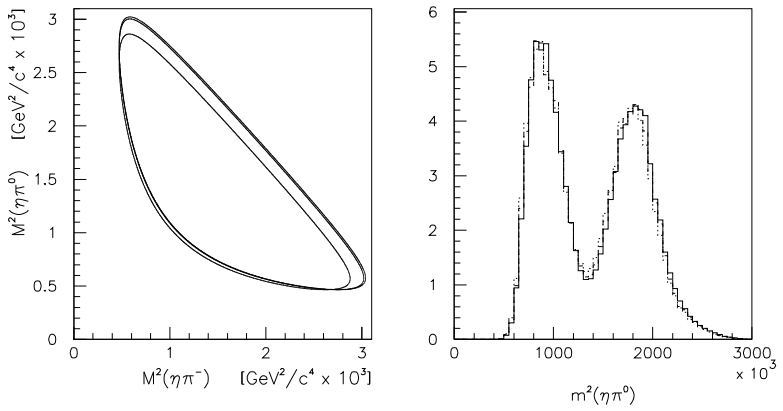

Figure 6: Phase space boundaries of the Dalitz plot for spectator momenta 0 and 100 MeV/c (which are hardly distinguishable) and for 300 MeV/c (left hand side). $M^2(\eta\pi^0)$ projection of a $a_2^-(1320)$ phase space distribution generated by a Monte Carlo simulation, for cuts at $P_{spec} = 0$, 100 and 300 MeV/c (full, dashed and dotted histogram, respectively, on the rhs.). The first two projections are hardly distinguishable.

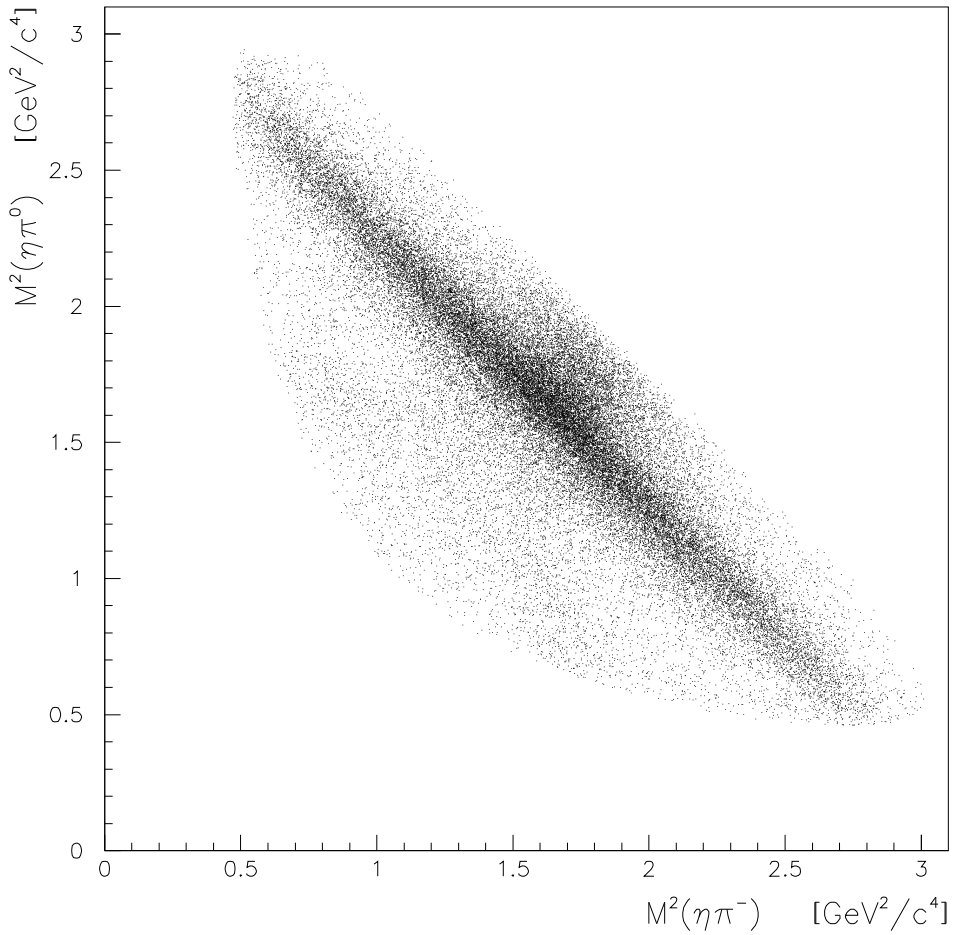

Figure 7: Dalitz plot for the annihilation channel $\pi^-\pi^0\eta$ (52.576 events, not acceptance corrected).

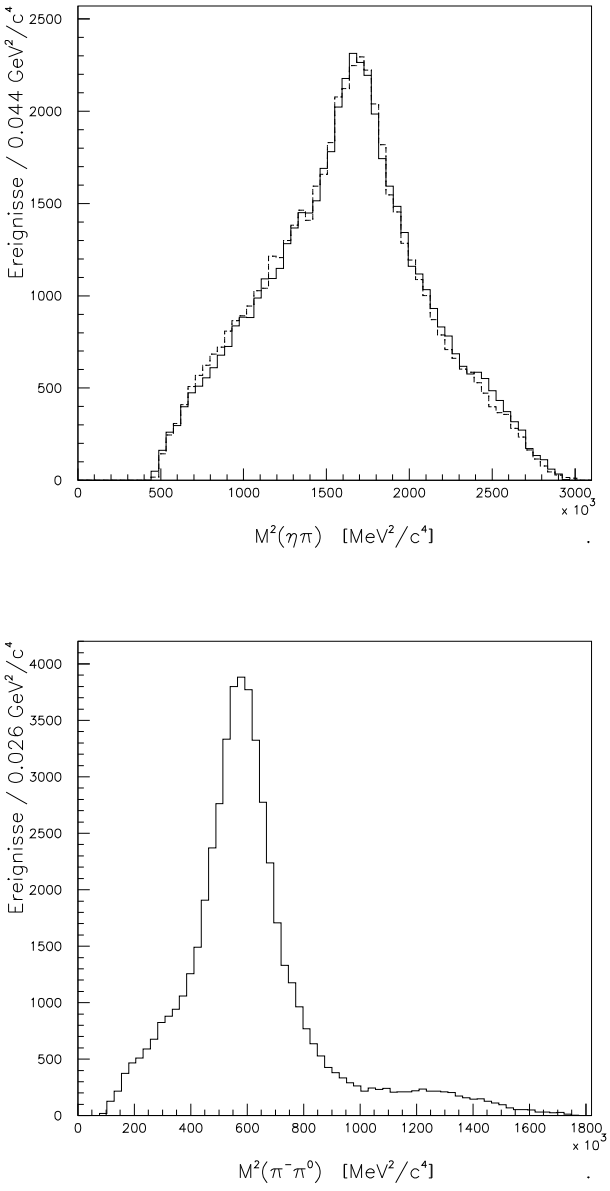

Figure 8: Projections of the above Dalitz plot. Full and dashed lines distinguish the histograms for $\eta\pi^0$ and $\eta\pi^-$, respectively

3 Monte Carlo Studies

3.1 Reconstruction Efficiencies

The program package CBGEANT was used, in combination with a deuteron event generator that simulates the spectator momentum distribution [8], to generate 1 627 398 phase-space distributed events of the type $\bar{\mathrm{p}}\mathrm{d} \to \pi^-\pi^0\eta + \mathrm{p}_{\mathrm{spectator}} \to \pi^- 4\gamma \mathrm{p}_{\mathrm{spect}}$. These were subjected to all selection cuts described in the previous chapter, including the 100 MeV/c cut on $\mathrm{P}_{\mathrm{spect}}$. An amount of 210 447 events passed all cuts, which gives a reconstruction efficiency $\epsilon = 12.9\%$ with uncertainty less than 0.1%.

3.2 Background

The following channels were considered as sources of possible background:

1-prong/4 γ:
$\pi^-\pi^0\pi^0$, $\pi^-\eta\eta$, $\pi^-\pi^0\eta'$

1-prong/5 γ (-1 undetected γ):
$\pi^-\pi^0\omega(\to \pi^0\gamma)$

1-prong/3 γ (+1 split-off):
$\pi^-\omega(\to \pi^0\gamma)$

1-prong/2 γ (+2 split-off):
$\pi^-\pi^0$, $\pi^-\eta$

2-prong/4 γ (-1 missing track):
$\bar{\mathrm{p}}\mathrm{d} \to \pi^-\pi^+\pi^0\eta + \mathrm{n}_{\mathrm{spect}}$

Phase-space distributed MC events were generated for each of these channels and the same selection criteria as for the present channel were applied to evaluate the background acceptance ϵ_{bg}. The contribution to the DP with $\mathrm{N_{DP}} = 52\,576$ was evaluated according to

$$\mathrm{N(background)} = \frac{\epsilon_{\mathrm{bg}}}{\epsilon_{\pi^-\pi^0\eta}} \cdot \frac{\mathrm{BR_{bg}}}{\mathrm{BR}(\pi^-\pi^0\eta)} \cdot \mathrm{N_{DP}} \quad ,$$

where $\mathrm{BR_{bg}}$ was taken from experiment [3] or was derived from the isospin 1 contributions in the related $\bar{\mathrm{p}}\mathrm{p}$ annihilation channels and where the appropriate secondary meson decay branchings are taken into account by the acceptances. The results are shown in Table 4 and in Fig.9. The total of all these background contributions to the DP amounts to 0.5%. In view of the small contributions of the individual background channels, even additional dynamical structures (instead of the used phase-space distributions) are not expected to produce significant structures in the final DP.

3.3 Acceptance Correction

Phase-space distributed MC events for $\bar{\mathrm{p}}\mathrm{d} \to \pi^-\pi^0(\to \gamma\gamma)\eta(\to \gamma\gamma)\mathrm{p}_{\mathrm{spect}}$ were generated for both JDCs, the old one used in the 1991 runs and the new one used in the 1994 run. Comparison by means of a χ^2 test showed no significant difference ($\chi^2/\mathrm{N}_{\mathrm{d.o.f}} = 413/396 = 1.04$) and hence both MC samples were combined to give a common acceptance.

In the acceptance distribution (Fig.10), structures are observed only close to the kinematic boundary. These are associated with the largest π^0 or π^- momenta or with π^- momentum below 50 MeV/c (upper edge in DP). In order to reduce the influence of purely statistical fluctuations, the acceptance DP containing 210 447 events was fitted with smooth, slowly varying functions (Fig.10, rhs). For the partial-wave analysis it was divided into the same bins as the experimental DP.

The experimental resolution and its influence on the acceptance was also studied by means of MC calculations. Fig.11 shows how events, originally contained in a pattern of rectangles distributed over the DP, are scattered when the original 4-vectors are kinematically fitted by our reconstruction procedure. The effect is largest in the center of the DP where a diagonal smearing is observed. It increases slightly the width of the $\mathrm{a}_2^{-/0}$ (see section 5) and it leads to a lower limit of the bin size for the analysis where kinematic broadening will not be taken into account explicitly.

background channel	generated events	selected events	$P_{spec} <$ 100 MeV/c	N_{bg}
$\pi^-\pi^0\pi^0$	80.000	23	5	68 ± 30
$\pi^-\eta\eta$	50.000	41	28	13 ± 2
$\pi^-\pi^0\omega$	80.000	238	107	119 ± 12
$\pi^-\pi^0\eta'$	50.000	124	80	7 ± 1
$\pi^-\omega$	50.000	40	15	23 ± 6
$\pi^-\pi^0$	20.000	0	0	< 2
$\pi^-\eta$	20.000	16	2	38 ± 27
$\pi^-\pi^+\eta\pi^0$	50.000		0	< 1

Table 4: Monte Carlo simulations of background channels. N_{bg} designates the expected number of background events in the present $\pi^-\pi^0\eta$ Dalitz plot with 52.576 events.

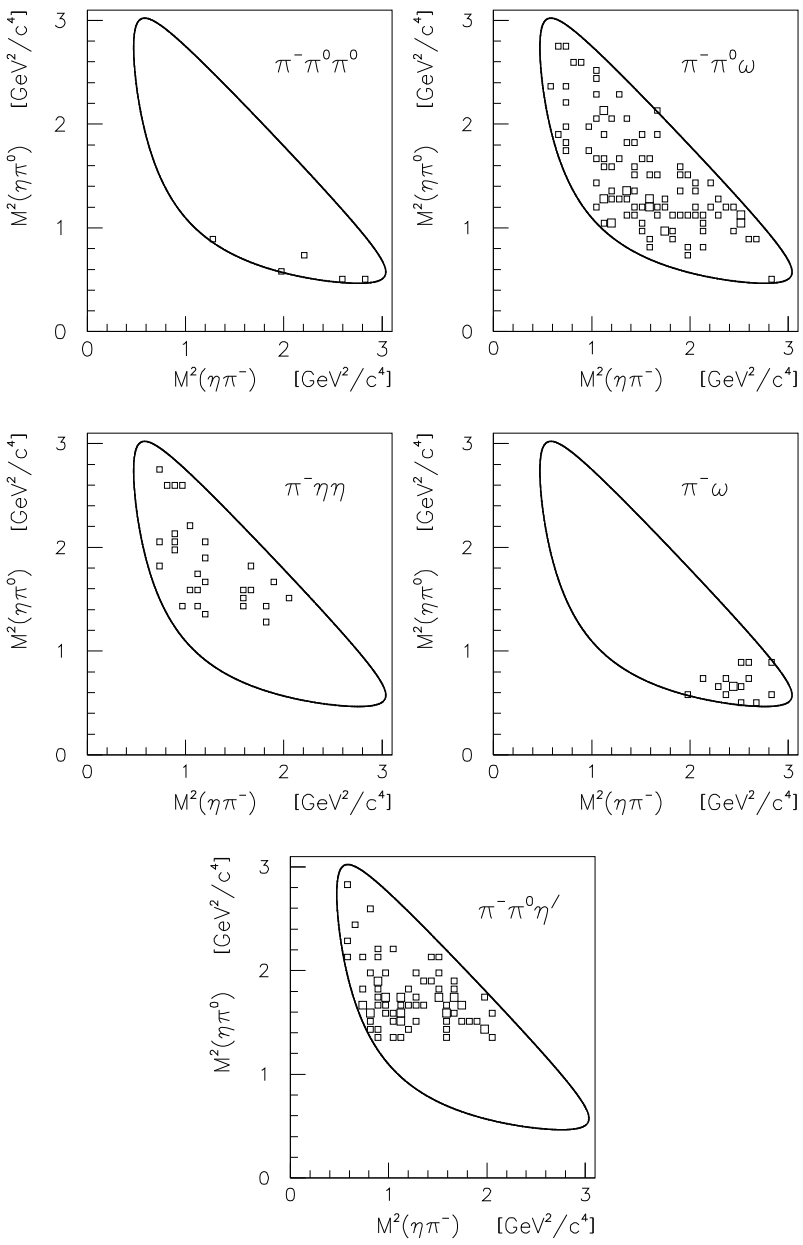

Figure 9: Distribution of reconstructed background events (column 4 of Table 4) in the $\pi^-\pi^0\eta$ Dalitz plot.

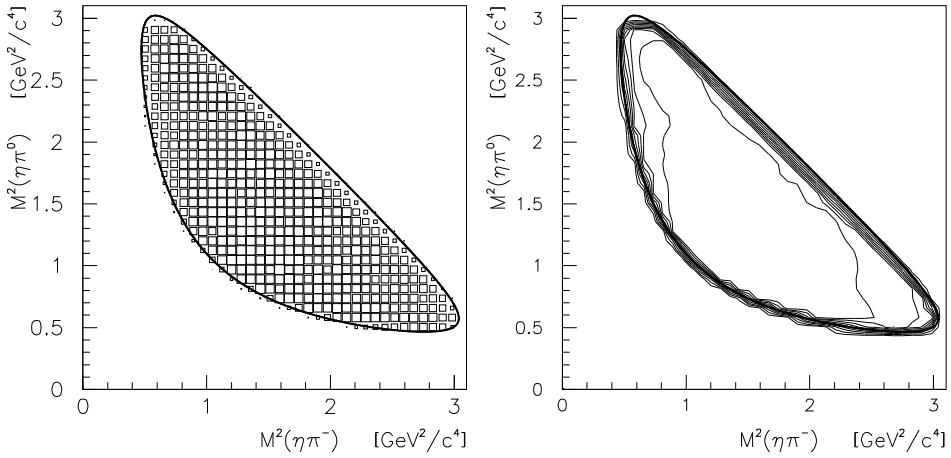

Figure 10: Binned acceptance Dalitz plot (l.h.s.) and contour plot of the smoothed acceptance Dalitz plot (r.h.s.).

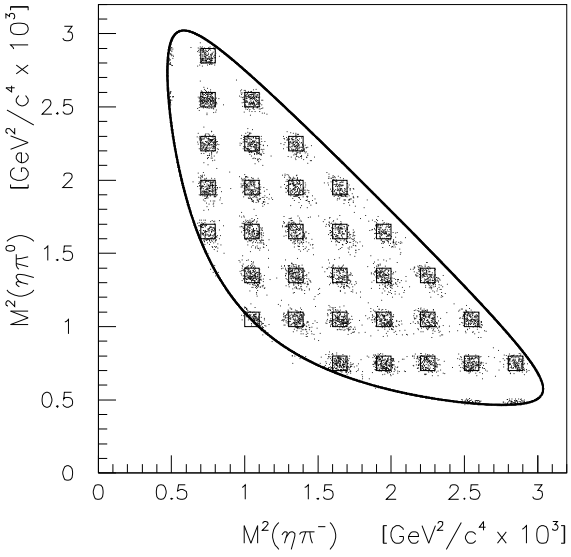

Figure 11: Scattering of reconstructed Monte Carlo events for an originally rectangular distribution.

4 Absolute Branching Ratio

Two independent methods, using different normalizations, were applied to derive the branching ratio for the present channel:

(i) Normalization to $\bar{\mathrm{p}}\mathrm{d} \to \pi^-\pi^0\mathrm{p}_{\mathrm{spec}}$.

The present 1-prong data were selected for $\pi^-\pi^0(\to \gamma\gamma)\mathrm{p}_{\mathrm{spec}}$ events in a separate analysis. In the same fashion as in Section 2 a very clean data sample of 57 228 events was obtained from a subsample of the total data that contained 48 261 $\pi^-\pi^0\eta\mathrm{p}_{\mathrm{spect}}$ events. With an acceptance $\epsilon' = 0.335 \pm 0.001$ for $\bar{\mathrm{p}}\mathrm{d} \to \pi^-\pi^0(\to \gamma\gamma)\mathrm{p}_{\mathrm{spec}}$, as obtained from a MC calculation, with the acceptance ϵ for $\pi^-\pi^0(\to \gamma\gamma)\mathrm{p}_{\mathrm{spec}}$ given above, and with the published [4] $\mathrm{BR}(\bar{\mathrm{p}}\mathrm{d} \to \pi^-\pi^0\mathrm{p}_{\mathrm{spec}}) = (4.0 \pm 0.5) \cdot 10^{-3}$, the BR of the present channel is determined by

$$\begin{aligned} \mathrm{BR}(\bar{\mathrm{p}}\mathrm{d} \to \pi^-\pi^0\eta\mathrm{p}_{\mathrm{spec}}) &= \frac{\mathrm{N}(\pi^-\pi^0(\to \gamma\gamma)\eta \to (\gamma\gamma)\mathrm{p}_{\mathrm{spec}})}{\mathrm{N}(\pi^-\pi^0(\to \gamma\gamma)\mathrm{p}_{\mathrm{spec}})} \\ &\quad \cdot\frac{\epsilon}{\epsilon'} \cdot \frac{1}{\mathrm{BR}(\eta \to \gamma\gamma)} \cdot \mathrm{BR}(\bar{\mathrm{p}}\mathrm{d} \to \pi^-\pi^0\mathrm{p}_{\mathrm{spec}}) \\ &= (6.6 \pm 0.8) \cdot 10^{-3} \end{aligned}$$

(ii) Normalization to $\bar{\mathrm{p}}\mathrm{n} \to \pi^-\mathrm{m}\pi^0$.

Analysis of bubble chamber experiments yielded $\mathrm{BR}(\bar{\mathrm{p}}\mathrm{n} \to \pi^-\mathrm{m}\pi^0, \mathrm{m} = 1, 2, 3...) = (16.4 \pm 0.5)\%$ [3,10], where the sum of all BR for $\bar{\mathrm{p}}\mathrm{n}$ annihilations is normalized to 100%. If we ignore the (probably weak) dependence of this definition on the spectator momentum cut and also ignore contributions from kaonic channels (see [3]), we can identify this BR with $\mathrm{BR}(\bar{\mathrm{p}}\mathrm{n} \to \text{1-prong})$. The reconstruction acceptance of the present $\pi^-\,\pi^0(\to \gamma\gamma)\,\eta(\to \gamma\gamma)\,\mathrm{p}_{\mathrm{spect}}$ channel for events with 1 long track was determined in a MC calculation: $\epsilon_1 = 0.146 \pm 0.003$. The restriction to long tracks should eliminate any influence of the electronic 1-prong trigger. Data selection for the June 1994 run yields $\mathrm{N} = 36\,257$ $\pi^-\,\pi^0(\to \gamma\gamma)\,\eta(\to \gamma\gamma)\,\mathrm{p}_{\mathrm{spect}}$ events for $\mathrm{N}_1 = 2\,860\,221$ 1-long track events, which leads to

$$\begin{aligned} \mathrm{BR}(\bar{\mathrm{p}}\mathrm{n} \to \pi^-\pi^0\eta) &= \frac{\mathrm{N}}{\mathrm{N}_1} \cdot \frac{1}{\epsilon_1} \cdot \frac{1}{\mathrm{BR}(\eta \to \gamma\gamma)} \cdot \mathrm{BR}(\bar{\mathrm{p}}\mathrm{n} \to \text{1-prong}) \\ &= (14.1 \pm 0.4) \cdot 10^{-3} \quad . \end{aligned}$$

Comparison of (i) and (ii) shows that the $\bar{\mathrm{p}}\mathrm{n}$ and $\bar{\mathrm{p}}\mathrm{p}$ capture rates are nearly equal, which is in agreement with a previous result on the triplett S-wave capture rates of $\bar{\mathrm{p}}\mathrm{n}$ and $\bar{\mathrm{p}}\mathrm{p}$ for $\bar{\mathrm{p}}$ stopped in liquid deuterium [11].

5 Partial Wave Analysis

5.1 Formalism and Method

The isobar-model transition amplitude is expressed by use of the Zemach formalism [12]. For an intermediate state decaying into 2 pseudoscalars with angular momentum ℓ, the amplitude for the transition of an initial ($\bar{\mathrm{p}}\mathrm{n}$) state with quantum numbers $\mathrm{I^G}$, $\mathrm{J^P}$ into a 3-body channel reads

$$\mathrm{A_{I^G,J^P}}(\vec{\mathrm{p}},\vec{\mathrm{q}}) = \sum_{\mathrm{I_3,L}} \mathrm{b_{I,I_3}} \cdot \mathrm{Z_{J^P,\ell,L}}(\vec{\mathrm{p}},\vec{\mathrm{q}}) \cdot \mathrm{F_{I_3,\ell}}(\vec{\mathrm{q}})$$

The spin-parity function Z describes the dependence on the angle between the decay momentum vectors $\vec{\mathrm{p}}$ and $\vec{\mathrm{q}}$ of the intermediate and of the secondary two-body systems, respectively. The isospin CG coefficients are $\mathrm{b_{1,0}} = 1/\sqrt{2}$ and $\mathrm{b_{1,-1}} = -1/\sqrt{2}$ for the $(\eta\pi^0)$ and the $(\eta\pi^-)$ intermediate systems, respectively. The dynamical amplitude F is factorized into a barrier-penetration factor $\mathrm{B}_\ell(\mathrm{q})$ [13] and a relativistic Breit-Wigner amplitude (see e.g. [14]):

$$\mathrm{F} = \alpha \cdot \mathrm{D_L(p,p_0)} \cdot \frac{\mathrm{m_0\Gamma_0 D}_\ell(\mathrm{q,q_0})/\rho(\mathrm{m_0})}{\mathrm{m_0^2 - m^2 - im_0 \cdot \Gamma(m)}}$$

with mass dependent width

$$\Gamma(\mathrm{m}) = \Gamma_0 \frac{\rho(\mathrm{m})}{\rho(\mathrm{m_0})} \mathrm{D}_\ell(\mathrm{q,q_0})^2$$

$$(\rho = 2\mathrm{q/m}, \mathrm{D}_\ell(\mathrm{q,q_0}) = \mathrm{B}_\ell(\mathrm{q})/\mathrm{B}_\ell(\mathrm{q_0})) \quad .$$

For fitting the data, a model space of intermediate two-meson resonances is assumed, each giving a rise to a reaction amplitude $\mathrm{A^j}$ of the form given above. The theoretical intensity is the incoherent sum of intensities from the $\bar{\mathrm{p}}\mathrm{n}$ initial states $^3\mathrm{S}_1$ and $^1\mathrm{P}_1$. These intensities are evaluated as DP cell integrals of coherent contributions from $\alpha_\mathrm{j} \mathrm{e}^{\mathrm{i}\varphi_\mathrm{j}} \mathrm{A^j}$. The real coefficient α_j and phase φ_j are fitted by minimizing

$$\chi^2 = \sum_{\mathrm{i=1}}^{\mathrm{N_{bin}}} \frac{(\mathrm{N_i \cdot c_i - N_i^{theor}})^2}{\sigma_\mathrm{i}^2} \quad ,$$

where $\mathrm{c_i}$ designates the acceptance correction for each cell. We will also give individual resonance strengths, obtained as the integral of $|\mathrm{A^j}|^2$ over phase space, divided by the integral of the squared magnitude of the total reaction amplitude. The program [15] employed for this analysis incorporates the CERN program MINUIT.

A DP cell area of $(7.75 \cdot 10^4\ \mathrm{MeV^2/c^4})^2$ was chosen. The insensitivity of our result on moderate variations of this area was checked empirically. Cells were not taken into account for fitting, if they extend over the phase space boundary, or if they contain less than 10 events, or if the acceptance correction $\mathrm{c_i}$ is larger than 2. In this way a number of 411 cells is obtained for fitting. The DP is not symmetrized with respect to π^-/π^0 in order to control the effects of possibly nonsymmetric background, or of acceptance corrections or of final-state interaction with the spectator proton. Some separate fits were also performed with the maximum likelihood program MAXTOOL [16] and good agreement was found.

5.2 Model Space

The allowed quantum numbers of intermediate resonances can be seen from Table 5. Of the established resonances [9] only $\rho^-(770)$ and $a_2^{0/-}(1320)$ can contribute in S-wave annihilation and, in addition, $a_0^{0/-}(980)$ in P-wave annihilation. Contributions from the ρ^- and $a_0^{0/-}$ resonances at 1450 MeV/c^2 (CB publications [4] and [7], respectively) are also admitted to the fit. Finally the data are investigated for evidence of the $\eta\pi$ P-wave. If not treated as free parameters (see below) the masses and widths of the quoted resonances (Tables 6 and 7) are taken from [9]. It is noted that only the $^3S_1$ and $^1P_1$ initial states contribute.

The characteristics of the separate squared amplitudes are gathered by Figs. 12-14. The a_2 bands generate, by interference, a blob above the ρ^-band (Fig. 12) which will be enhanced by the additional interference with ρ^- in the total annihilation amplitude. Annihilation from P-wave enables enhancements in the vicinity of the phase-space boundaries (Fig. 13). Since the experimental DP shows no indication of the sharp $a_0^{0/-}(980)$ bands and since the resulting limit on such contributions is rather independent on variations of the width, we have not attempted an investigation of threshold effects in terms of a Flatte-parametrization. The intensities of an assumed $\eta\pi$ P-wave resonance (" $\widehat{\rho}$") overlap strongly with those of the a_2 and ρ^-. S- and P-wave annihilation, leading to $\widehat{\rho}$, are distinguished by intensity maxima in the center or edges of the DP, respectively (Fig. 14).

final state	$I^G(J^P)$	L	ℓ	initial state $^3S_1$	$^1P_1$
$(\pi^0\pi^-)_S\,\eta$	$1^+(0^+)$	1	0	P	•
$(\pi^0\pi^-)_P\,\eta$	$1^+(1^-)$	0	1	P	•
		1	1	•	P
		2	1	P	•
$(\pi^0\pi^-)_D\,\eta$	$1^+(2^+)$	1	2	P	•
		2	2	•	P
$(\eta\pi^{0-})_S\,\pi^{-0}$	$1^-(0^+)$	1	0	P	•
$(\eta\pi^{0-})_P\,\pi^{-0}$	$1^-(1^-)$	0	1	P	•
		1	1	•	P
		2	1	P	•
$(\eta\pi^{0-})_D\,\pi^{-0}$	$1^-(2^+)$	1	2	P	•
		2	2	•	P

Table 5: Allowed transitions of the $\bar{p}n$ system into $\pi^-\pi^0\eta$. Quantum numbers $I^G(J^P)$ refer to the intermediate two-meson system. L designates its angular momentum with respect to the third meson and ℓ its decay angular momentum. P = forbidden by parity.

	J^P	m $[MeV/c^2]$	Γ $[MeV/c^2]$
$\rho(770)$	1^-	769	151
$\rho(1450)$	1^-	1465 ± 25	310 ± 60

Table 6: Intermediate $\pi^-\pi^0$ resonances ($I^G = 1^+$, PDG values)

	$J^{P(C)}$	m $[MeV/c^2]$	Γ $[MeV/c^2]$
$a_2(1320)$	$2^{+(+)}$	1318	107 ± 5
$a_0(980)$	$0^{+(+)}$	983	$50 - 100$
$a_0(1450)$	$0^{+(+)}$	1450 ± 40	270 ± 40

Table 7: Intermediate $\eta\pi$ resonances ($I^G = 1^-$, PDG values)

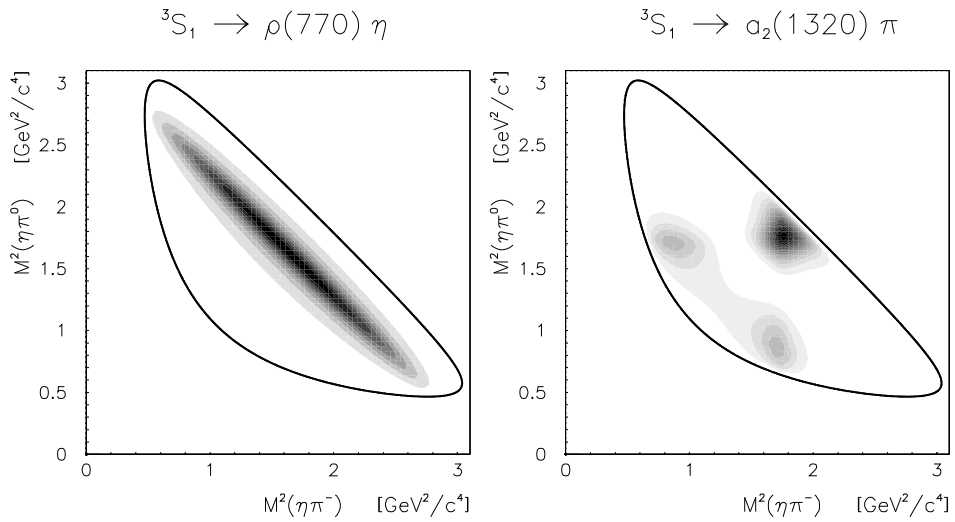

Figure 12: Amplitude squared for the two dominant resonances in $\bar{p}d$ S-wave annihilation into $\pi^-\pi^0\eta$.

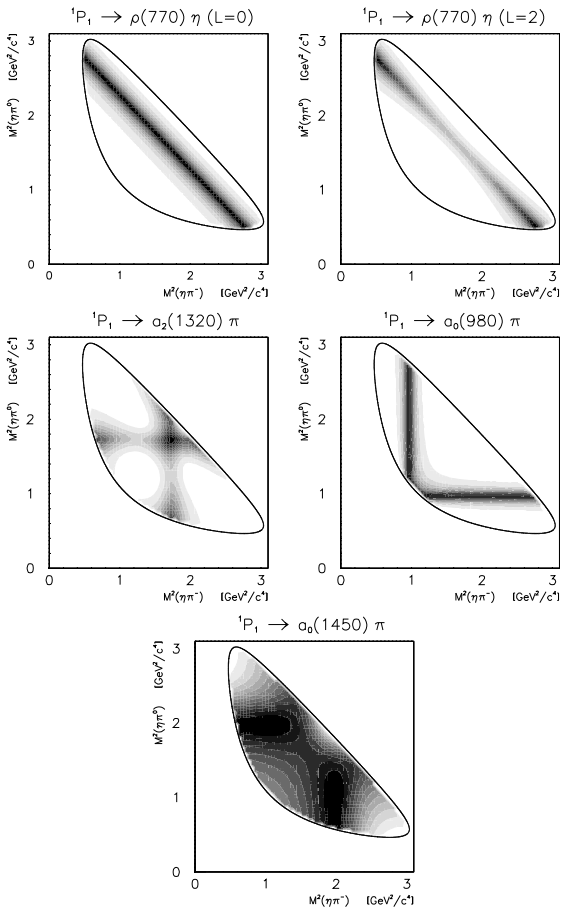

Figure 13: Amplitude squared for contributions from $\bar{p}n$ P-wave.

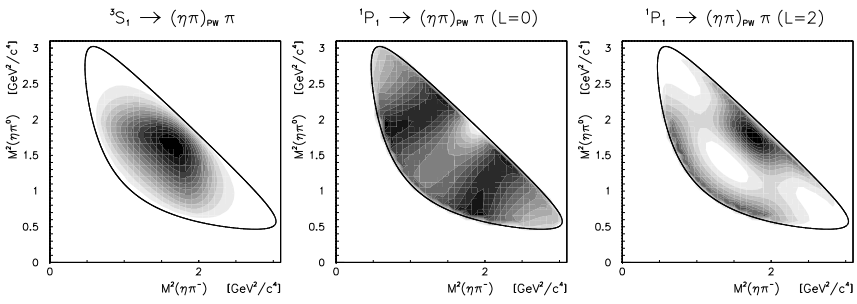

Figure 14: Amplitude squared for a $\eta\pi$ resonance with $J^P = 1^-$, mass 1400 MeV/c^2, width 300 MeV/c^2 from $\bar{p}n$ S- and P-wave.

5.3 Results

Model I:

$$\begin{aligned} \bar{\mathrm{p}}\mathrm{n}(^3\mathrm{S}_1) &\rightarrow \rho(770)\eta \ , \\ \bar{\mathrm{p}}\mathrm{n}(^3\mathrm{S}_1) &\rightarrow \mathrm{a}_2(1320)\pi \ . \end{aligned}$$

The minimal model with these two obvious contributions gives only a qualitative description of the DP: $\chi^2/\mathrm{N_{d.o.f}} = 7.1$. Broad structures in the distribution of χ^2 give evidence for the insufficiency of this model [1].

Model II ($^1\mathrm{P}_1$ included):

$$\begin{aligned} \bar{\mathrm{p}}\mathrm{n}(^1\mathrm{P}_1) &\rightarrow [\rho(770)\eta]_{\mathrm{L}=0} \\ &\rightarrow [\rho(770)\eta]_{\mathrm{L}=2} \\ &\rightarrow \mathrm{a}_2(1320)\pi \\ &\rightarrow \mathrm{a}_0(980)\pi \\ &\rightarrow \mathrm{a}_0(1450)\pi \end{aligned}$$

The fit is strongly improved: $\chi^2/\mathrm{N_{d.o.f}} = 3.07$ however, clear structures remain in the distribution (Fig. 15). These show up as two islands of too much theoretical intensity in the $\mathrm{a}_2^{0/-}$ regions and as a modulation in the $\rho(770) - \mathrm{a}_2$ interference region. The individual intensities (Table 8) show a considerable $^1\mathrm{P}_1$ initial-state contribution. However, a vanishing intensity is found for $\mathrm{a}_0(980)$. An extension of this model by inclusion of $\rho(1450)$ [4] did not lead to a significant improvement of the fit. Such a contribution, with fitted intensities below 3%, is not taken into account below.

In a second version of this model (IIb) the $\rho(770)$ and $\mathrm{a}_2(1320)$ resonance parameters were treated as free parameters (Table 9). An improvement of $\chi^2/\mathrm{N_{d.o.f}}$ (by 0.4) is achieved for the price of a rather high ρ-mass and certainly too high mass (1340 MeV/c^2) and too large width (161 MeV/c^2) for the a_2, which indicates that the fit tries to compensate for missing other contributions. The same explanation may hold for the relatively large $\mathrm{a}_0(1450)$ strength, as compared to the vanishing $\mathrm{a}_0(980)$ strength, in both versions of this model. Treating the $\mathrm{a}_0(1450)$ parameters as free led to divergent fits.

Modifications of the $\rho(770)$ and $\mathrm{a}_2(1320)$ line shape

Since prominent χ^2 structures appear in the wings of the a_2 and ρ^- bands, the influence of line shapes was studied in Models I and II. However, it should be kept in mind that

the differences between theoretical and experimental distributions are normalized to the statistical error in the χ^2 plots, which makes differences most significant in regions of high intensity in the DP.

To study the influence of the dominant $\rho\pi$ decay of the a_2, the mass dependence of the width was modified [17]:

$$\Gamma(\mathrm{m}) = \frac{\rho(\eta\pi)}{\rho_0(\eta\pi)}\mathrm{D}_2(\mathrm{q}_{\eta\pi})^2\Gamma_{\eta\pi} + \frac{\rho(\rho\pi)}{\rho_0(\rho\pi)}\mathrm{D}_2(\mathrm{q}_{\rho\pi})^2\Gamma_{\rho\pi} \quad ,$$

where ρ(xy) designates the 2-body phase-space factor 2q/m. The partial widths obey the equation $\Gamma_0 = \Gamma_{\eta\pi} + \Gamma_{\rho\pi}$. The resulting energy dependence is found to be significant only close to the $\rho\pi$ threshold, where the amplitude is strongly suppressed, however, due to the small a_2 width and to centrifugal damping, such that no significant net effect remains.

The radius parameter R that appears in the damping factors B_ℓ(q) was varied around the standard value of 1 fm, between 0.6 and 1.4 fm, which causes small changes in the Breit-Wigner amplitude [1] without affecting the χ^2 distribution in a significant manner.

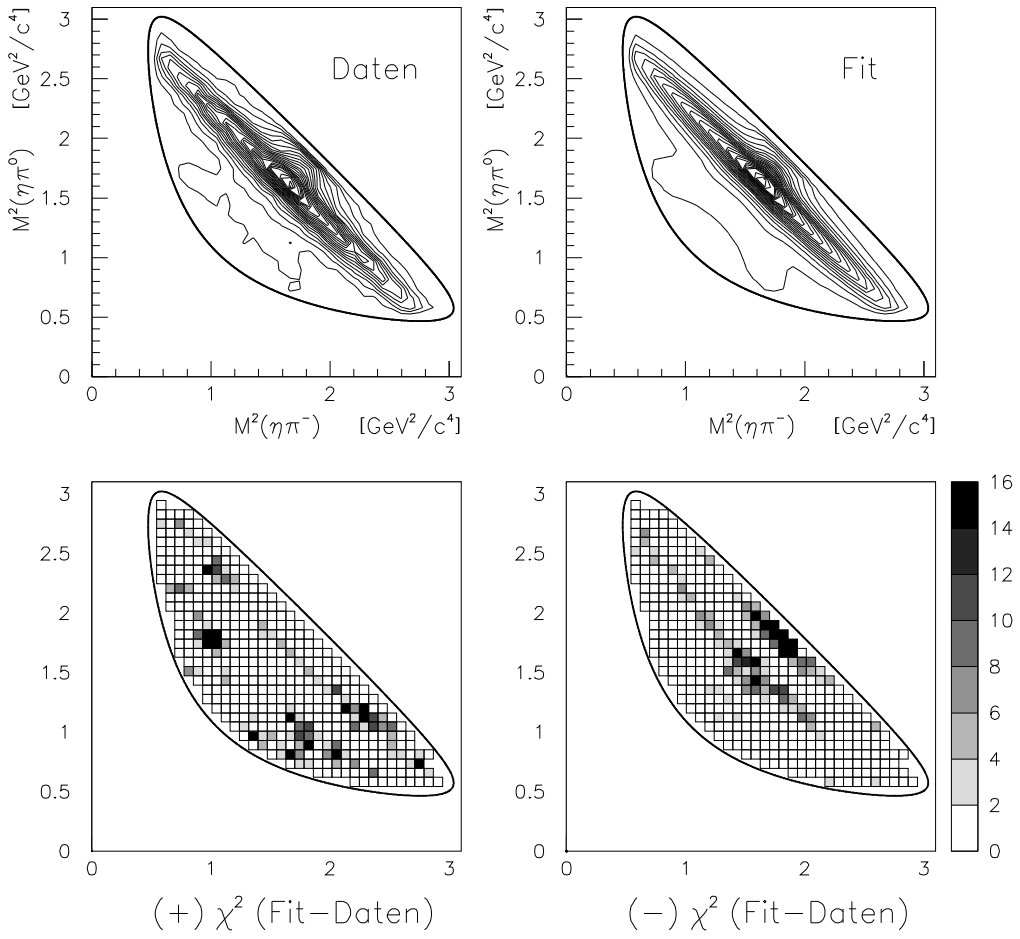

Figure 15: Comparison of data and fit for model IIa.

initial state		intensity	$\|\alpha\|$	ϕ
$^3S_1$		**67.7 %**		
	$\rho(770)$	58.3 %	13.4 ± 0.2	0°
	$a_2(1320)$	5.6 %	3.0 ± 0.1	28° ± 3°
$^1P_1$		**32.3 %**		
	$\rho(770)$(L=0)	5.2 %	4.6 ± 0.4	0°
	$\rho(770)$(L=2)	1.8 %	1.9 ± 0.2	265° ± 5°
	$a_2(1320)$	11.1 %	7.8 ± 0.1	184° ± 4°
	$a_0(980)$	0.0 %	0.2 ± 0.1	188° ± 28°
	$a_0(1450)$	5.7 %	1.9 ± 0.1	34° ± 4°
$\chi^2/N_{d.o.f.} = 1223/(411-12) = 3.07$				

Table 8: Results of the fit for model IIa. The $a_0(980)$ width was fixed to $\Gamma = 54\,\mathrm{MeV/c^2}$, but the results are not sensitive to variations between 50 and $100\,\mathrm{MeV/c^2}$.

initial state		intensity	$\|\alpha\|$	ϕ
$^3S_1$		**67.0 %**		
	$\rho(770)$	56.0 %	13.1 ± 0.2	0°
	$a_2(1320)$	8.0 %	3.1 ± 0.1	37° ± 2°
$^1P_1$		**33.0 %**		
	$\rho(770)$(L=0)	5.3 %	4.9 ± 0.3	0°
	$\rho(770)$(L=2)	1.7 %	1.7 ± 0.2	272° ± 5°
	$a_2(1320)$	13.9 %	7.3 ± 0.2	176° ± 4°
	$a_0(980)$	0.0 %	0.2 ± 0.1	171° ± 24°
	$a_0(1450)$	6.2 %	1.9 ± 0.2	14° ± 4°
$\chi^2/N_{d.o.f.} = 1063/(411-16) = 2.69$				

	mass [MeV/c^2]	width [MeV/c^2]
$\rho(770)$	786 ± 1	151 ± 2
$a_2(1320)$	1340 ± 3	161 ± 5

Table 9: Same as Table 8, but free fit of the $\rho(770)$ and $a_2(1320)$ resonance parameters (model IIb).

Model III ($(\eta\pi)$ P-wave included):

The $\eta\pi$ P-wave with exotic quantum numbers $J^{P(C)} = 1^{-(+)}$, parameterized as a BW resonance, is allowed in the transitions

$$\begin{aligned} \bar{p}n(^3S_1) &\rightarrow (\eta\pi)_P\pi \\ \bar{p}n(^1P_1) &\rightarrow [(\eta\pi)_P\pi]_{L=0} \\ \bar{p}n(^1P_1) &\rightarrow [(\eta\pi)_P\pi]_{L=2} \end{aligned}$$

No a_0 resonances are taken into account in this model. The parameters of $\rho^-(770)$ and $a_2(1320)$ are kept fixed at the PDG values in model IIIa and taken to be free in model IIIb. The improvement of the fit is considerable: $\chi^2/N_{d.o.f.} = 1.42$ in case IIIa (c.f. 3.07 in case IIa) and 1.29 in case IIIb (c.f. 2.69 in case IIb).

The χ^2 distribution (Fig. 16) does not show structures any more (c.f. Fig 15) but just statistical fluctuations. All contours in Fig. 15 can be traced back to interference of the $(\eta\pi)$ P-wave with $\rho^-(770)$ and $a_2(1320)$ (see Fig. 17).

For model IIIb the binned theoretical DP is shown in Fig.18 and the detailed fit results are listed in Table 10. The total $(\eta\pi)_P$ intensity amounts to 11%, with almost vanishing contribution from the $^1P_1 \rightarrow (\eta\pi)_P\pi$ L = 2 transition. The parameters obtained for $\rho^-(770)$ and $a_2(1320)$ are almost compatible with the PDG values. The small excess in the a_2 width can be explained by the effect of the experimental resolution. In Gaussian approximation, we have $\Gamma = \sqrt{8\ \ln 2}\sqrt{\sigma^2_{exp} + \sigma^2_0}$, which yields an experimental resolution $\sigma_{exp} \approx 20$ MeV/c^2, in good agreement with the MC calculations (Sect. 3.3)

The contribution from the $^1P_1$ initial state amounts to about 1/3 of the total intensity. Its significance is obvious when the fit is repeated without allowing for this initial state (Fig.19). Comparison with Fig.13 is suggestive of missing $^1P_1$-contributions. Comparison of the upper with the lower panels of Fig.19 shows that these relative contributions increase with increasing spectator momentum, as expected for the annihilation dynamics.

Model IV ($\eta\pi$ P-wave and a_0 resonances included):

In an extension of model IIIa (ρ^- and a_2 resonance parameters fixed) the resonances $a_0(980)$ and $a_0(1450)$ are introduced to the fit. To reduce the number of free parameters, the $(\eta\pi)_P\pi$, L=2 contribution (see above) was set to zero. The results (Table 11) confirm the smallness of a_0 contributions and their negligible influence on the $\eta\pi$ P-wave parameters. The omission of $a_0(980)$ or $a_0(1450)$ in this model reduces the fit quality insignificantly, yielding $\chi^2/N_{d.o.f} = 514/397$ or $512/397$, respectively.

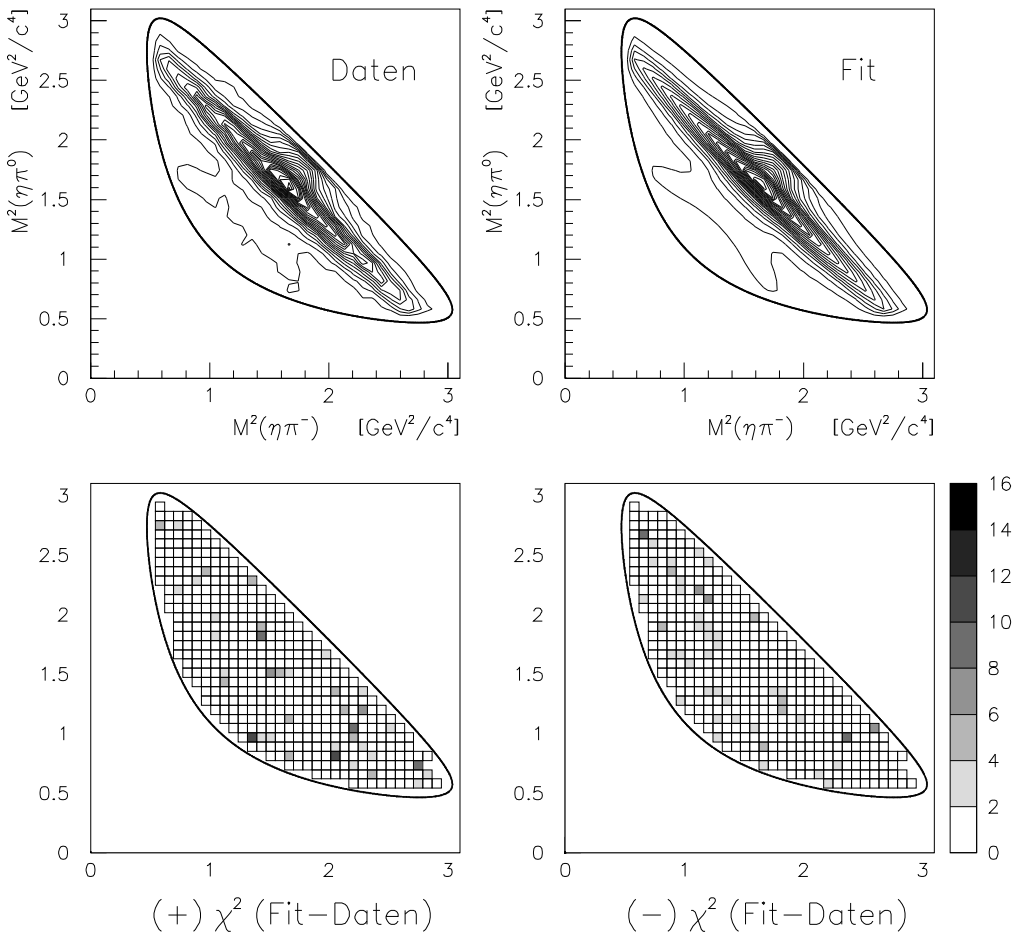

Figure 16: Comparison of data and fit for model IIIb.

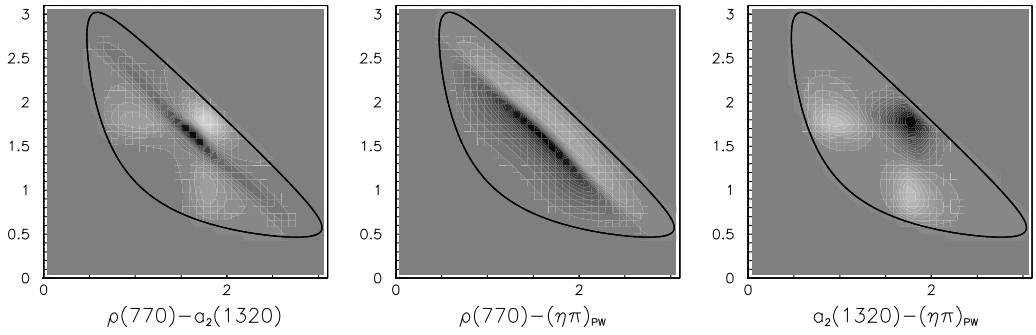

Figure 17: Interference terms of the dominant fit amplitudes of model IIIb.

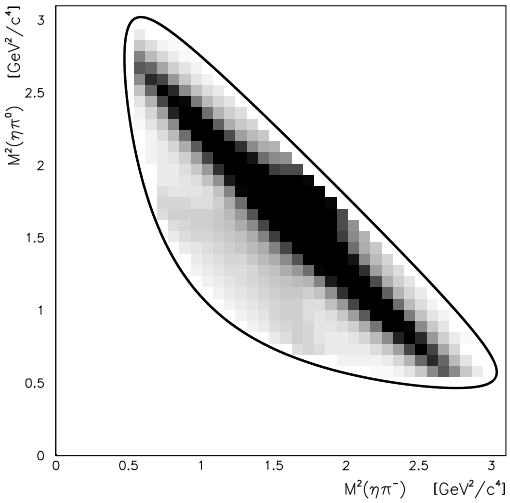

Figure 18: Theoretical DP for model IIIb (binned version of the upper right panel of Fig. 16). Maximal blackness corresponds to more than 250 events/bin.

initial state		intensity	$\|\alpha\|$	ϕ
$^3S_1$		**66.4 %**		
	$\rho(770)$	30.0 %	9.9 ± 0.6	0°
	$a_2(1320)$	16.7 %	3.3 ± 0.1	7° ± 8°
	$(\eta\pi)_{PW}$	7.9 %	2.1 ± 0.1	213° ± 5°
$^1P_1$		**33.6 %**		
	$\rho(770)$(L=0)	10.3 %	6.4 ± 1.0	0°
	$\rho(770)$(L=2)	17.3 %	5.7 ± 0.6	146° ± 10°
	$a_2(1320)$	3.8 %	4.2 ± 0.4	315° ± 25°
	$(\eta\pi)_{PW}$ (L=0)	2.8 %	1.6 ± 0.4	68° ± 34°
	$(\eta\pi)_{PW}$ (L=2)	0.5 %	0.5 ± 0.3	109° ± 40°
$\chi^2/N_{d.o.f.} = 506/(411-20) = 1.29$				

	mass [MeV/c^2]	width [MeV/c^2]
$\rho(770)$	777 ± 1	144 ± 3
$a_2(1320)$	1320 ± 3	124 ± 8
$(\eta\pi)_{PW}$	1398 ± 20	309 ± 50

Table 10 : Results of the fit using model IIIb. The given errors are those of the minimization evaluated by use of the MINOS program.

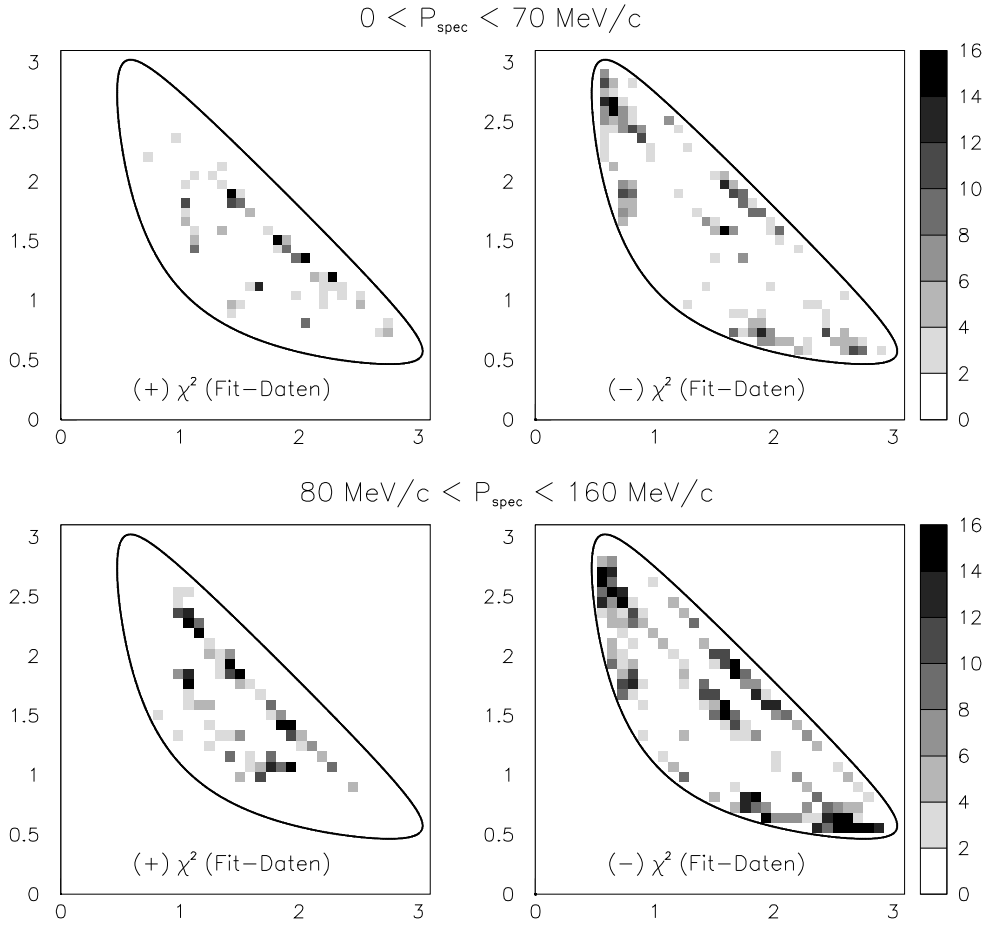

Figure 19: χ^2 distribution for a fit where the ${}^1P_1$ contribution are omitted from model IIIb.

initial state		intensity	$\|\alpha\|$	ϕ
$^3S_1$		**67.7 %**		
	$\rho(770)$	32.1 %	10.2 ± 0.6	0°
	$a_2(1320)$	11.8 %	4.2 ± 0.1	7° ± 5°
	$(\eta\pi)_{PW}$	6.6 %	1.9 ± 0.1	202° ± 4°
$^1P_1$		**32.3 %**		
	$\rho(770)$(L=0)	7.9 %	5.6 ± 0.9	0°
	$\rho(770)$(L=2)	17.1 %	5.6 ± 0.4	159° ± 11°
	$a_2(1320)$	3.2 %	3.9 ± 0.5	327° ± 18°
	$(\eta\pi)_{PW}$ (L=0)	3.9%	1.9 ± 0.2	90° ± 23°
	$a_0(980)$	0.0 %	0.2 ± 0.1	286° ± 34°
	$a_0(1450)$	0.1 %	0.3 ± 0.2	115° ± 46°
$\chi^2/N_{d.o.f.} = 509/(411-26) = 1.29$				

Table 11: Results of the fit using model IV

5.4 Resonance Characteristics of the ($\eta\pi$) P-wave

To simulate a nonresonant ($\eta\pi$) P-wave in model IIIb, the width of the BW amplitude was fixed to a very large value (Γ= 1 GeV/c^2). The fit gets worse ($\Delta\chi^2$= 114) and yields a rather large $^1P_1$ intensity that would be hard to accept (Table 12). Fig.20 shows the corresponding χ^2 distribution. Scans of the width yield a well-defined, but rather broad minimum of χ^2 (Fig.21). In these scans the $(\eta\pi)_P$ L=2 contribution is fixed to zero (see above).

As an alternative to the BW amplitude, an effective-range Ansatz was tried. For energy s and angular momentum ℓ=1 of the $\eta\pi$ system, the expansion of the scattering phase [18] leads to the production amplitude

$$F = \alpha \cdot B_L \cdot \frac{q/\sqrt{s}}{a + bq^2 - iq^3/\sqrt{s}} \quad .$$

This amplitude can be transformed into a BW amplitude for a $>$ 0, b $<$ 0, but it may also adopt a nonresonant form. The fit turned out to diverge for a large set of start parameters in the range of nonresonant solutions(a, b $>$ 0). However, for start parameters in the vicinity of the above resonance solution, the fit converges and good agreement with the solution for model IIIb is established (Table 13). The shape of the amplitude and the Argand plot (Fig. 22) fulfill the expectations for a resonance solution. This is not a trivial result, since the fit is open to nonresonant solutions.

A survey of PWA fits I-IV is presented in Table 14. The evidence for the presence of ($\eta\pi$) P-wave contributions is very clear, in particular from the detailed comparison of models II and III (see above). If these contributions are parameterized as resonances, very satisfactory fits are obtained, and widths Γ $>$ 500 MeV/c^2 are excluded. The effective range parametrization lends support to the resonance description.

The best values of the resonance parameters resulting from these PWA studies are those given in Table 10. In addition to the purely statistical (MINOS) errors given there, systematic errors were extracted by varying the following fit conditions: smoothing of the acceptance distribution, binning of the DP, cuts on the spectator momentum. Of these the latter are found to have the largest influence on the resonance parameters but the variations are still smaller than the statistical errors. Significant changes of χ^2 occur only for cuts above 160 MeV/c. It is expected that the background contribution increases with P_{spec} (see Table 4). Final state interactions should have the same tendency. Both effects will be associated with a π^-/π^0 asymmetry of the DP, which is however not observed below 160 MeV/c. The fit results for three different momentum cuts, dividing the momentum distribution in 3 equal parts, and the effects of the other variations mentioned above, allow for an estimate of the systematic errors of the resonance parameters. In this way we arrive at the following resonance parameters:

$$m = (1400 \pm 20_{stat} \pm 10_{syst}) \mathrm{MeV/c^2}$$

$$\Gamma = (310 \pm 50_{stat}\ ^{+40}_{-20_{syst}}) \mathrm{MeV/c^2} \quad .$$

Initial state		intensity	$\|\alpha\|$	ϕ
$^3S_1$		**41.5 %**		
	$\rho(770)$	9.3 %	5.5 ± 0.5	0°
	$a_2(1320)$	14.6 %	3.3 ± 0.1	10° ± 3°
	$(\eta\pi)_{PW}$	7.1 %	1.2 ± 0.1	205° ± 4°
$^1P_1$		**58.5 %**		
	$\rho(770)$(L=0)	40.8 %	12.6 ± 0.3	0°
	$\rho(770)$(L=2)	4.5 %	2.9 ± 0.2	174° ± 8°
	$a_2(1320)$	4.9 %	4.8 ± 0.3	225° ± 5°
	$(\eta\pi)_{PW}$ (L=0)	1.6 %	0.9 ± 0.1	7° ± 7°
$\chi^2/N_{d.o.f.} = 635/(411-12) = 1.59$				

Table 12: Results for a modification of model IIIb where a fixed width $\Gamma = 1\,\mathrm{GeV/c^2}$ is assumed for the $\eta\pi$ P-wave.

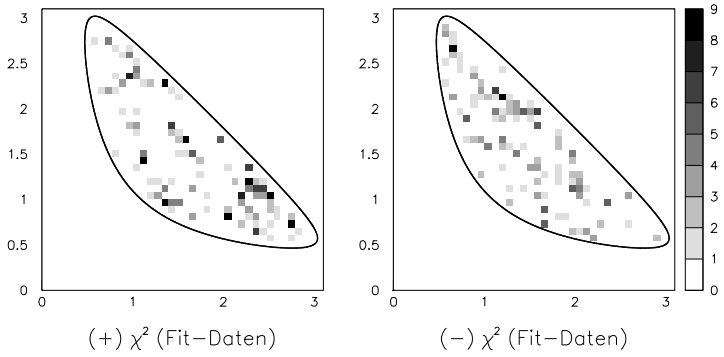

Figure 20: χ^2 distribution corresponding to Table 10.

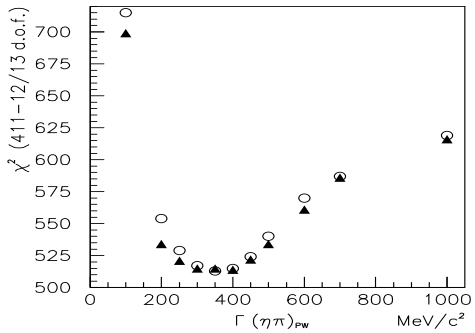

Figure 21: Dependence of χ^2 on the resonance width of the $\eta\pi$ P-wave for a fixed mass of $1398\,\mathrm{MeV/c^2}$ and for fitted mass (circles and triangles, respectively).

Anfangs-zustand		Intensität	ϕ
$^3S_1$		**66.8 %**	
	$\rho(770)$	30.6 %	0°
	$a_2(1320)$	10.9 %	10° ± 5°
	$(\eta\pi)_{PW}$	7.9 %	225° ± 3°
$^1P_1$		**33.1 %**	
	$\rho(770)$(L=0)	8.6 %	0°
	$\rho(770)$(L=2)	18.9 %	157° ± 10°
	$a_2(1320)$	3.8 %	331° ± 18°
	$(\eta\pi)_{PW}$ (L=0)	2.9%	100° ± 20°
	$(\eta\pi)_{PW}$ (L=2)	0.5%	42° ± 29°
$\chi^2/N_{d.o.f.} = 509/(411-16) = 1.29$			

Table 13: Results of a fit using an effective range parametrization for the $\eta\pi$ P-wave instaed of the BW amplitude in model IIIb.

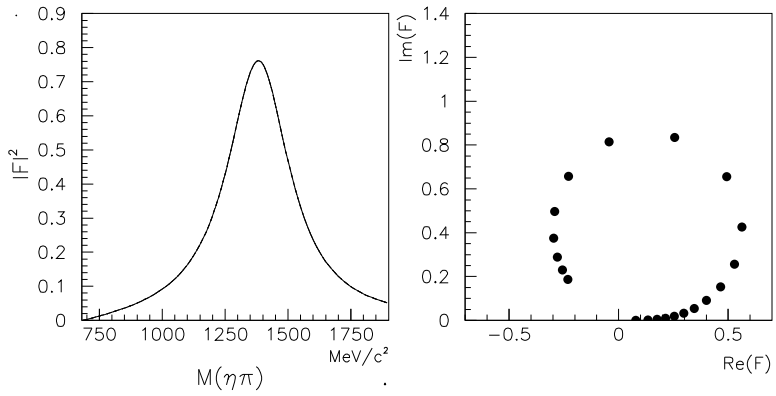

Figure 22: Lhs.: effective range amplitude (without factor $B_L(p)$) corresponding to the fit results in Table 13. Rhs.: Corresponding Argand plot with equidistant points in the range $690 \leq E(\mathrm{MeV/c^2}) \leq 1800$ (arbitrary global scaling).

	I	IIa	IIb	IIIa	IIIb	IV
$^3S_1$	•	•	•	•	•	•
$^1P_1$		•	•	•	•	•
$\rho(770)$	•	•	free	•	free	•
$a_2(1320)$	•	•	free	•	free	•
$a_0(980)$		•	•			•
$a_0(1450)$		•	•			•
$(\eta\pi)_{PW}$				free	free	•
$\chi^2/d.o.f.$	2916/(411-3) = 7.15	1223/(411-12) = 3.07	1063/(411-16) = 2.69	559/(411-16) = 1.42	506/(411-20) = 1.29	509/(411-26) = 1.32

Table 14: Survey of the fits using BW amplitudes

References

[**1**] K. Hüttmann, diploma thesis (Munich, Feb. 1997)

[**2**] W. Roethel, diploma thesis (Munich, 1995)

[**3**] J. Sedlak and V. Simak, Sov.J.Part.Nucl. 19 (1988) 191

[**4**] A.Abele et al., (CB collaboration) preprint (1996);
C. Strassburger, CB-Note 245 (1996)

[**5**] M.Benayoun et al., CB-Note 280 (1996)

[**6**] M.Benayoun, Minutes of the CB Meeting, March 1995

[**7**] C.Amsler et al., (CB collaboration), Phys. Lett. B333 (1994) 277

[**8**] C.Strassburger, CB-Note 188 (1994)

[**9**] PDG: Review of Particle Properties, Phys.Rev. D54 (1996) 1

[**10**] A.Bettini et al., Nuovo Cimento 47 (1967) 642

[**11**] R.Bizzari, Nuovo Cimento 53 (1968) 956

[**12**] C.Zemach, Phys.Rev. B140 (1964) 97, 109;
P.Baillon, in Meth. of Subnucl. Phys., edited by K.Nikolic,
publ. by Gordon and Breach (Herzeg-Novi 1968)

[**13**] J.M.Blatt und V.F.Weisskopf, Theoretical Nuclear Physics, Wiley (New York 1952)

[**14**] S.U.Chung et al., Ann. d. Physik 4 (1995) 404

[**15**] S.Spanier, program COPAWA, CB-Note 297 (1996)

[**16**] C.Felix, program MAXTOOL, in Ph.D. thesis (Munich 1997)

[**17**] B.S.Zou, private communication

[**18**] J.Pisut and M.Roos, Nucl.Phys. B6 (1968) 325;
S. Gasiorowicz, Elementary Particle Physics, Wiley (New York 1996)